Enhanced dissimilar aluminum alloy joints using 0.1 mm offset in refill friction stir spot welding

José Francisco Caldeira Maranho [a,b], Fan Cui [c,d,*], Huawei Tang [c,d], Xiaosong Feng [d], Hao Luan [d], Junjun Shen [b], Witor Wolf [e], Brenda Juliet Martins Freitas [f], Wenya Li [c], Nelson Guedes de Alcântara [f,g], Jorge Fernandez dos Santos [b], Benjamin Klusemann [b,h], Guilherme Yuuki Koga [f,g,**]

[a] Postgraduate Program in Materials Science and Engineering, Federal University of São Carlos, Rod. Washington Luís, km 235, São Carlos, SP, 13565-905, Brazil
[b] Helmholtz-Zentrum Hereon, Institute of Materials Mechanics, Solid State Materials Processing, Max-Planck-Str. 1, Geesthacht, 21502, Germany
[c] State Key Laboratory of Solidification Processing, Shanxi Key Laboratory of Friction Welding Technologies, Northwestern Polytechnical University, Xi'an, 710072, China
[d] Shanghai Aerospace Equipments Manufacturer, Huaning Road 100, Shanghai, 200245, China
[e] São Carlos School of Engineering-EESC, University of São Paulo-USP, São Carlos, 13563-120, Brazil
[f] Federal University of São Carlos, Department of Materials Engineering, Rod. Washington Luís, km 235, São Carlos, SP, 13565-905, Brazil
[g] Federal University of São Carlos, Center for Characterization and Development of Materials (CCDM), Rod. Washington Luís, km 235, São Carlos, SP, 13565-905, Brazil
[h] Leuphana University of Lüneburg, Institute for Production Technology and Systems, Universitätsallee 1, Lüneburg, 21335, Germany

ARTICLE INFO

ABSTRACT

5A06-O and 2219-T87 aluminum alloys are promising candidates for propellant tanks. In this study, refill friction stir spot welding (refill FSSW) with a 0.1 mm offset was applied to produce defect-free 5A06-O/2219-T87 welds. A Box-Behnken method and statistical analysis were used to optimize the processing parameters, by determining the influence of welding parameters on lap shear strength (LSS). Plunge depth was the most influential parameter on LSS. All joints failed through the weld seam, including those tested at −55 °C. Microhardness measurements showed a slight increase in the 5A06 sheet over time, while the 2219 sheet exhibited significant hardness reduction. Microstructural analysis revealed typical features of refill FSSW, including a heat-affected zone, thermo-mechanically affected zone, stir zone, hook, and joint-line remnants. Novel findings include the identification of an onion structure in the welds, characterized by fine equiaxed grains and nanoprecipitates that contribute to weld's hardness. This unique microstructure, formed under the thermal and mechanical conditions of the FSSW process, strengthens the material and enhances its mechanical performance. Stop-action tests provided insights into material flow and microstructural evolution during welding. While conventional refill FSSW could not produce defect-free welds, the findings highlight the potential of the 0.1 mm offset refill FSSW to enhance weld quality, supporting its application in aerospace components requiring high mechanical integrity across extreme temperature ranges.

1. Introduction

Aluminum alloys have been widely applied in the transportation industries to reduce structural weight and fuel consumption. Among them, the 5A06 stands out given the high strength-to-weight ratio and corrosion resistance, being applied in automotive, shipbuilding and aerospace sectors [1–3]. The 5A06 alloy belongs to the Al–Mg system, with Mg content ranging from 5.8 to 6.8 wt%, leading to the formation of Al_3Mg_2 precipitates within the aluminum matrix. In contrast, the 2219 Al-alloy is also characterized by its high ductility and outstanding cryogenic properties, making it widely used in propellant tanks, being exposed to very low temperatures [4–7].

Despite their excellent properties, most aluminum alloy joints produced by conventional welding techniques often display issues related to porosity, liquation and solidification cracks [8–11], compromising the quality and the mechanical strength of critical engineering components. Refill Friction Stir Spot Welding (refill FSSW), a solid-state joining technique derived from Friction Stir Welding (FSW), has emerged as a suitable alternative to overcome defects associated with fusion welding processes. The process has successfully been applied to join both similar and dissimilar materials, including Al/Al [12–17], Mg/Mg [18,19], Al/Mg [20,21], Al/Ti [22–24], Al/Steel [25,26], and Mg/Steel [27–29]. Compared to the classical Friction Stir Spot Welding (FSSW), the main advantage of refill FSSW is the complete refilling of the weld, since in FSSW the tool lefts an exit hole at the end of process, which may act as a stress and corrosion concentrator [30], compromising the weld performance and durability.

The refill FSSW process uses a cylindrical non-consumable tool constituted of three independent components: a clamping ring, a shoulder, and a probe. Fig. 1a shows the overlapped sheets hold tightly by the clamping ring to avoid escaping of plasticized material during the process. Shoulder and probe start to rotate and, due to an axial force, the shoulder is forced against the top sheet up to a predetermined plunging depth, while the probe is simultaneously retracted, Fig. 1b, ensuring enough room according to plastic incompressibility. The plasticized material, heated from friction between the shoulder and the material surface, flows into the cavity created by the probe retraction. When the preset depth is reached, the shoulder moves upward and the probe moves towards, returning to surface level, Fig. 1c. This step of the process forces the plasticized material, which was occupying the cavity, to fill the hole left by the shoulder. After the welding cycle is complete, the tool is removed, Fig. 1d.

However, despite its advantages, refill FSSW can still lead to some welding defects, such as lack of mixing, incomplete refill, and voids formation [31–35]. The main reasons for the appearance of these defects are: i) insufficient material flow during the refilling stage ascribed to an inappropriate parameters combination, ii) weak metallurgical bonding caused by different heat cycles and thermal gradients during welding, and iii) material loss due to stuck material between the threads in the outer surfaces of shoulder and probe. Xu et al. [30] and Zhao et al. [32] successfully eliminated the aforementioned defects using a surface indentation of 0.3 and 0.2 mm of the probe on the last welding step, respectively. Recent investigations have also correlated processing

parameters with joint quality and defect formation in refill FSSW. Ferreira et al. [35] investigated the occurrence of internal defects in welded samples of dissimilar aluminum alloys produced by refill FSSW by applying statistical analysis, which identified rotational speed as a key factor influencing defect formation, in which low rotational speed reduced material flowability, leading to refilling defects and compromising the weld strength. Tier et al. [36] evaluated the impact of the processing parameters on the microstructure and shear strength of 5042 aluminum alloy joints produced by refill FSSW, in which they observed that reducing the rotational speed from 1900 rpm to 900 rpm increased the bonding ligament length, leading to stronger joints.

While these studies have significantly advanced the understanding of parameter influence on weld performance, research on refill FSSW of 5A06-O/2219-T87 aluminum alloys remains unexplored. This alloys combination presents challenges due to their distinct hardening mechanisms, solid solution and grain refinement, and precipitation hardening. Understanding how the welding parameters influence mechanical properties, microstructural evolution, and joint performance is critical for optimizing the use of this technique in aerospace and cryogenic applications.

This work investigates the welding parameters influence on lap shear strength (LSS) through the Box-Behnken Design (BBD). Furthermore, the microstructure, thermal cycle and mechanical properties were analyzed using a 0.1 mm offset. This offset consists, during the refilling stage, to retract the shoulder up to 0.1 mm below the surface level and to plunge the probe up to 0.1 mm below the surface level, which creates a small indentation on the welding surface (Fig. 1e and f), while in conventional refilling stage both shoulder and probe return exactly to the surface level, Fig. 1c and d.

2. Materials and methods

2.1. Aluminum alloys 5A06-O and 2219-T87

Al-sheets were used in this work: 3 mm-thick 5A06-O and 4 mm-thick anodized 2219-T87. 5A06 is a non-heat treatable alloy, where the O temper designation consists of annealing followed by rapid quenching. AA2219 is a heat treatable alloy, and the temper T87 consists of solution heat treatment, cold working and artificial aging. The typical chemical composition ranges of the Al-alloys are presented in Table 1.
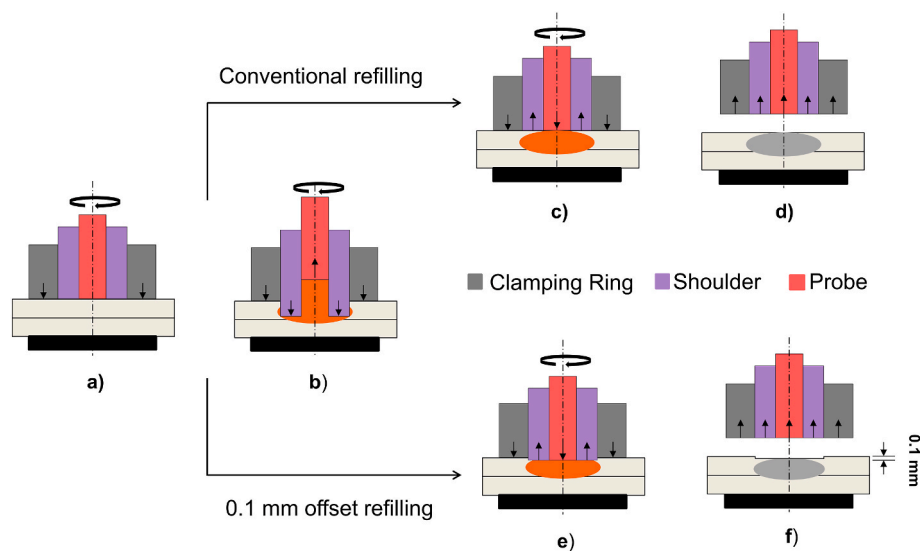

Fig. 1. Schematic illustration of the conventional and the 0.1 mm offset refill FSSW process through the shoulder plunge variant. a) Clamping stage and initial tool rotation, b) shoulder plunging and probe retraction, c) shoulder and probe's returning to surface level, d) tool removal, e) refilling stage, showing the shoulder retraction up to 0.1 mm below the surface level and the probe plunging up to 0.1 mm below the surface level, f) welding joint with 0.1 mm indentation on the surface.

Table 1
Reference for chemical composition (wt%) of 5A06-O and 2219-T87 aluminum alloys.

Material	Cu	Mg	Mn	Zn	Si	Fe	Ti	Zr	V
5A06-O	≤0.1	5.8–6.8	0.5–0.8	≤0.2	≤0.4	≤0.4	0.02–0.1	–	–
2219-T87	5.8–6.8	≤0.02	0.2–0.4	≤0.1	≤0.2	≤0.3	0.02–0.1	0.1–0.25	0.05–0.15

2.2. Welding process

The welds were produced using the Harms & Wende® RPS200 machine (Fig. 2) through the shoulder plunge variant with a 0.1 mm offset. The 0.1 mm offset was applied to further enhance defect mitigation, as conventional refill FSSW resulted in voids, compromising joint integrity. The welding tool consists of a 9-mm-diameter shoulder made of tungsten carbide cobalt alloy, a 6-mm-diameter probe, and a 17-mm-diameter clamping ring made of Hotvar tool steel. Both probe and shoulder have threads on their outer surfaces to improve the material flow.

Thermal cycle measurements were carried out using 0.5-mm-diameter K-type thermocouples, positioned 0.2 mm below the welding interface. The holes were located at 0, 3.75, and 5.9 mm distance from the welding center, corresponding to regions affected by the probe, the shoulder, and the clamping ring, respectively, to obtain the temperature distribution in the main regions of the weld and, consequently, assist in the study of the weld's metallurgical behavior.

2.3. Design of Experiments

Box-Behnken Design, a response surface methodology (RSM), and analysis of variance (ANOVA) were used as statistical analysis tools to evaluate the influence of process parameters on the lap shear strength. This methodology was selected as it provides a comprehensive dataset while requiring only a small number of experiments. Furthermore, recent works [31,37–39] have showed that BBD is suitable and effective approach to optimize the processing parameters in solid state joining processes. A total of 15 runs were performed to correlate the lap shear strength and welding parameters to obtain an optimal parameter combination that maximizes the lap shear strength of the weld. Rotational Speed (RS), Plunge Depth (PD) and Plunge Speed (PS) were chosen as the main parameters. The variation in rotational speed allows the evaluation of the frictional heating and material plasticization, while plunge depth allows the evaluation of the material consolidation, and the plunge speed influences heat input and may help to prevent abrupt

material deformation. Dwell time (DT) was kept constant at 1 s for all parameter combinations to maintain consistency and eliminate its variability as a factor in the analysis. The main welding process parameters and their levels are detailed in Table 2. The statistical analysis was performed via Minitab® 19 software.

2.4. Mechanical testing

LSS tests were performed using a universal testing machine Zwick/Roell® 1478 with a load capacity of 100 kN, and displacement speed of 1 mm/min at room temperature. The specimens used are schematically presented in Fig. 3. Four replicates of the optimized condition were also tested: two at room temperature and two at low temperature (-55 °C). The fracture surfaces of the optimized condition were analyzed by scanning electron microscope (SEM) for both temperatures in a FEI Quanta 400 microscope. Vickers hardness measurements were conducted using Struers® DuraScan machine, according to ASTM E384-17. Two hardness profiles were made in the cross-section of the weld: one in the middle of top sheet, i.e., in 5A06 and the other one in the middle of the bottom sheet, i.e. in AA2219. The applied load, indentation time and distance between each indentation were 0.1 kg, 10 s and 0.15 mm, respectively. Hardness profiles were performed in as-welded condition and after 1, 4 and 7 days after welding to evaluate the natural aging effect.

2.5. Microstructural characterization

To reveal the grain structure in the different welding zones, the cross-sections of the welds were prepared according to standard metallographic procedure, electrolytically etched with Barker solution at 20 V for 60 s, and subsequently analyzed using a Leica® DM IRM optical microscope (OM) coupled with polarized light. A TESCAN MIRA scanning electron microscope coupled with Energy-Dispersive X-ray Spectroscopy (EDS) detector was employed to characterize the intermixed layers located on shoulder path of the optimized condition weld.

Transmission Electron Microscopy (TEM) analysis was conducted using a FEI Tecnai G2–20 TEM equipped with a Field Emission Gun (FEG) source, operating at 200 kV, and an EDS detector for compositional analysis. The TEM sample was prepared via a Focused Ion Beam (FIB) system integrated into a dual-beam scanning electron microscope (Quanta 3D FEI SEM) featuring a Ga-ion source, ensuring precise and site-specific specimen extraction.

Stop-action experiments were carried out to visualize the material flow behavior and understand the formation of defects during both the plunging and refilling stages of the process. A stop-action experiment consists in interrupting the welding operation at a specific plunge depth by pressing the emergency stop button. Immediately after the interruption, the welds were rapidly quenched in cold water to preserve their microstructure features at the moment of interruption. For the plunging stage, the process was halted at 1, 2 and 3 mm plunge depths, allowing the visualization of the material flow evolution as the tool penetrated

Fig. 2. Harms & Wende® RPS200 machine used to produce welds in this work.

Table 2
Welding process parameters and their levels employed.

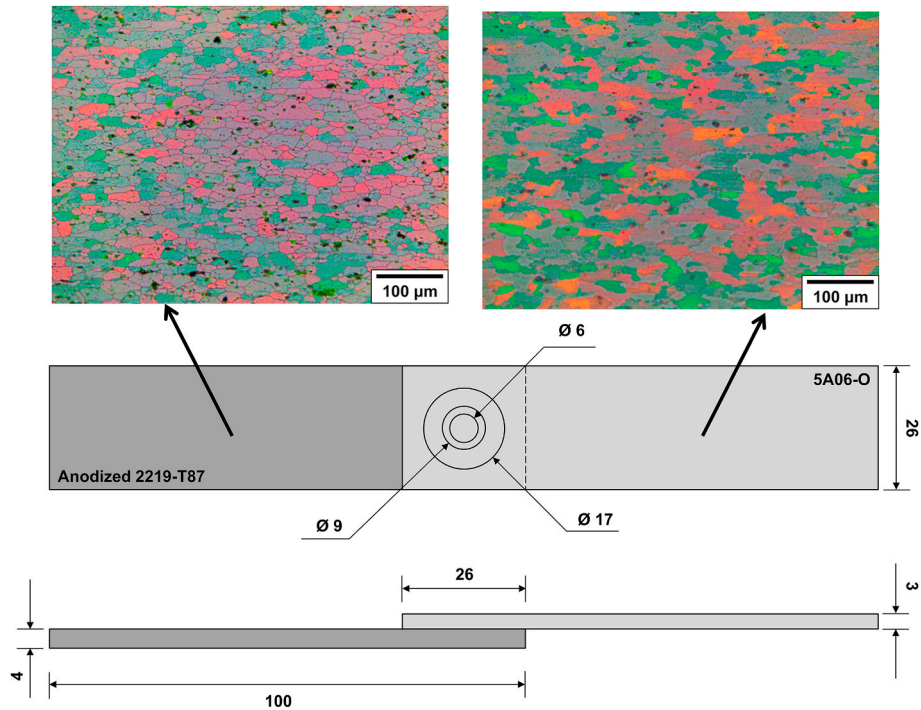| Parameters	Levels		
	−1	0	1
Rotational speed (rpm)	1000	1500	2000
Plunge speed (mm/s)	1	1.5	2
Plunge depth (mm)	2.8	3	3.2

Fig. 3. Schematic illustration of the refill FSSW specimen for the lap shear test and the microstructure transverse to the rolling direction of each base material. Dimensions in mm.

the material. For the refilling stage, stop-action experiments were performed for both the conventional refill process and the 0.1 mm offset refill process. In these experiments, the process was interrupted at 2, 1, and 0.1 mm below the top sheet surface, enabling a comparative assessment of material redistribution under different travel factors (TS) conditions. The main difference between these two variants lies in the travel factor (TS), which represents the ratio between probe retraction and shoulder plunging. In the conventional process, this parameter is set at 1.25 based on the tool geometry. However, in the offset refill process, the 0.1 mm offset applied to the probe and shoulder alters this ratio, as described by Equation (1):

$$TS = \frac{(3.75 - (-0.1))}{(3 - 0.1)} \qquad \text{(Eq. 1)}$$

In Equation (1), the +0.1 mm term indicates the probe penetration depth relative to the weld surface, while the −0.1 mm term denotes the shoulder position below the top sheet surface. As a result, the TS value increases from 1.25 to 1.33, leading to an increase in probe speed and, consequently, changes in the material flow dynamics during refilling. The parameters combination used for stop-action tests was rotational speed (RS) = 1500 rpm, plunge speed (PS) = 1 mm/s and dwell time (DT) = 1 s. The specific plunge depths at which the welding process was interrupted are summarized in Table 3.

3. Results and discussion

3.1. Process parameters optimization

The contribution of the welding parameters on LSS was evaluated through the ANOVA (Table 4) and response surface graphs (Fig. 4). As shown in Table 4, the model has a coefficient of determination (R^2) of 85.48% and an adjusted coefficient of determination (adj-R^2) of 74.58%, indication of good fitting between the experimental and the predicted responses. Once the confidence level adopted was $\alpha = 0.05$, all the three parameters were significant for the model. The contribution of RS (Rotational Speed), PS (Plunge Speed) and PD (Plunge Depth) was 9.70%, 15.52% and 49.76%, respectively. As reported in other works [13,36], PD is commonly one of the most significant parameters on LSS for refill FSSW because of its influence on metallurgical bonding between the top and the bottom sheets as there is no melting in refill FSSW.

Fig. 4a indicates how the LSS values vary between PS and RS,

Table 3
Shoulder and probe positions during stop-action tests with and without offset. Sample ID refers to Fig. 10.

Sample ID	Shoulder Position (mm)	Probe Position (mm)	
10(a)	1	−1.25	**Plunging stage**
10(b)	2	−2.5	
10(c)	3	−3.75	
10(d)	2	−2.5	**Conventional refilling stage**
10(e)	1	−1.25	
10(f)	0.1	0.1	
10(g)	2	−2.42	**0.1 mm offset refilling stage**
10(h)	1	−1.09	
10(i)	0.1	0.1	

Table 4
Analysis of variance. SS = sum of squares; DF = degrees of freedom; MS = mean square.

| Source	SS	DF	MS	F Value	p value	Contribution (%)
Model	8,353,628	6	1,392,271	7.85	0.005	85.48
RS	948,450	1	948,450	5.35	0.050	9.70
PS	1,517,012	1	1,517,012	8.55	0.019	15.52
PD	4,863,285	1	4,863,285	27.41	0.001	49.76
RS*RS	378,623	1	378,623	1.87	0.208	3.87
PD*PD	268,150	1	268,150	1.51	0.254	2.74
RS*PD	378,108	1	378,108	2.13	0.182	3.87
Error	1,419,496	8	177,437			14.52
Lack of fit	1,006,011	6	167,668	0.81	0.644	10.29
Pure Error	413,485	2	206,743			4.23
Total	9,773,124	14				100
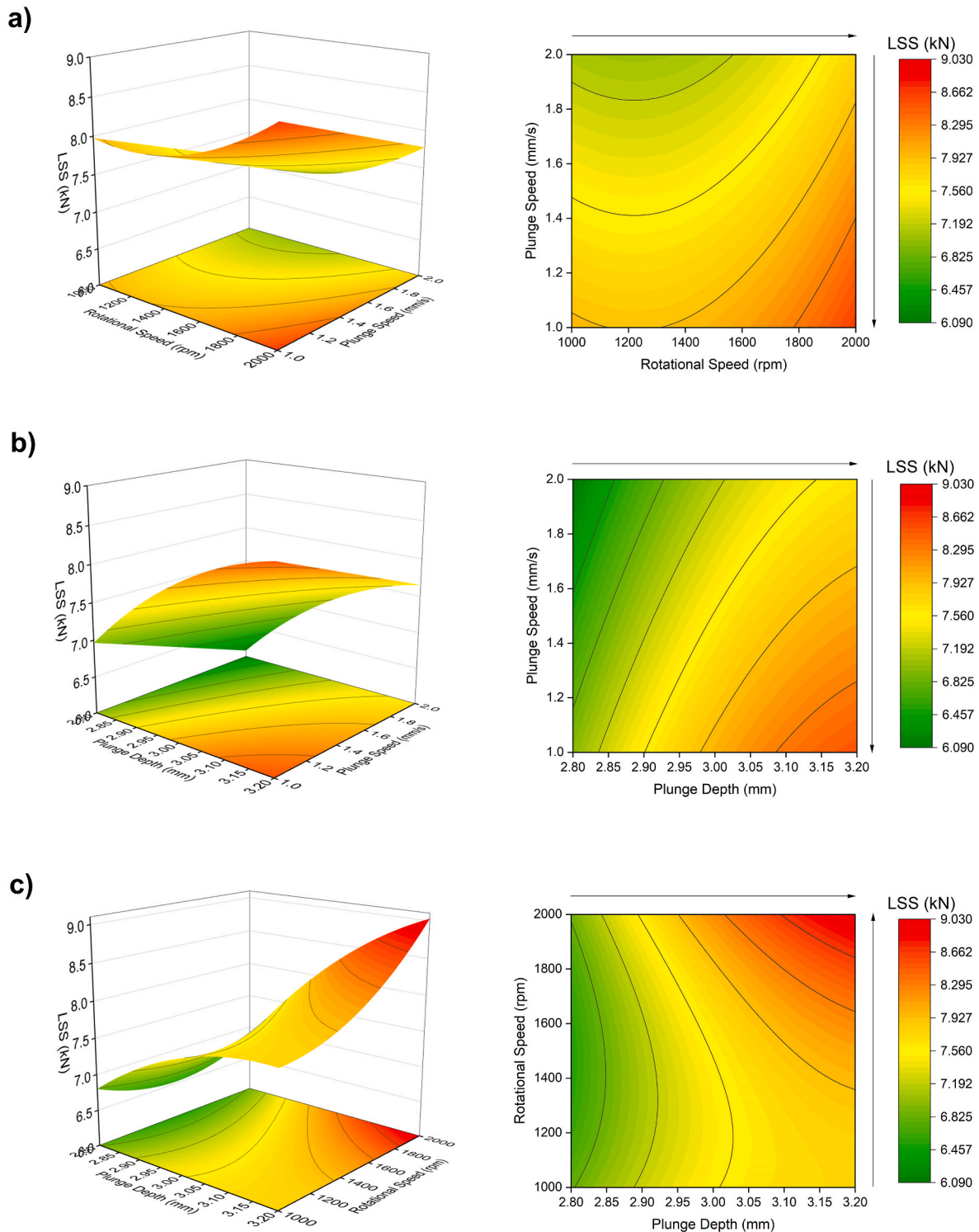
Fig. 4. Response surface graphs and contour plots of welding parameters influence on LSS. a) RS x PS with fixed value of PD at 3 mm, b) PD x PS with fixed value of RS at 1500 rpm and c) PD x RS with fixed value at PS at 1.5 mm/s.

keeping the PD constant at 3 mm (level 0). Increasing the RS up to 2000 rpm and decreasing the PS up to 1 mm/s, the LSS value continuously increases. When low RS and high PS were employed, the welds resulted in weaker properties due to the insufficient heat input, i.e., poor plasticized material flowability, and shorter time to accommodate the plasticized material. The relationship of PS and PD, with RS constant at 1500 rpm (level 0), is shown in Fig. 4b. Increasing the PD up to 3.2 mm and decreasing the PS up to 1 mm/s, LSS increases since PD shows a

great influence on metallurgical bonding in the weld. Fig. 4c displays the relationship between RS and PD, with PS constant at 1.5 mm/s (level 0). As aforementioned, RS and PD are the two most significant parameters on LSS. Increasing RS up to 2000 rpm and PD up to 3.2 mm, the LSS also increases. After analyzing the response surface graphs and the contour plots, the optimized welding parameters were identified as RS = 2000 rpm, PD = 3.2 mm and PS = 1 mm/s, and the predicted LSS value was 9.5 kN. The LSS can be determined by Equation (2):

$$LSS\,(kN) = \frac{-47748 - 12.13{\cdot}RS - 871{\cdot}PS + 39590{\cdot}PD + 0.001197{\cdot}RS{\cdot}RS - 6717{\cdot}PD{\cdot}PD + 3.07{\cdot}RS{\cdot}PD}{1000}$$

(Eq. 2)

To check this prediction, four confirmative tests were performed: two at room temperature and two at low temperature (−55 °C), since the material combination in this study aims to be applied in propellant tanks. The results of the confirmatory LSS tests at room and low temperatures were 10.8 ± 0.6 kN and 11.9 ± 0.7 kN, respectively. The LSS at low temperature was higher in comparison to the LSS at room temperature. This behavior can be attributed to a decrease in thermal activation, reducing the dislocations' mobility and resulting in higher LSS. In the following, only results produced via the optimized process parameters are discussed.
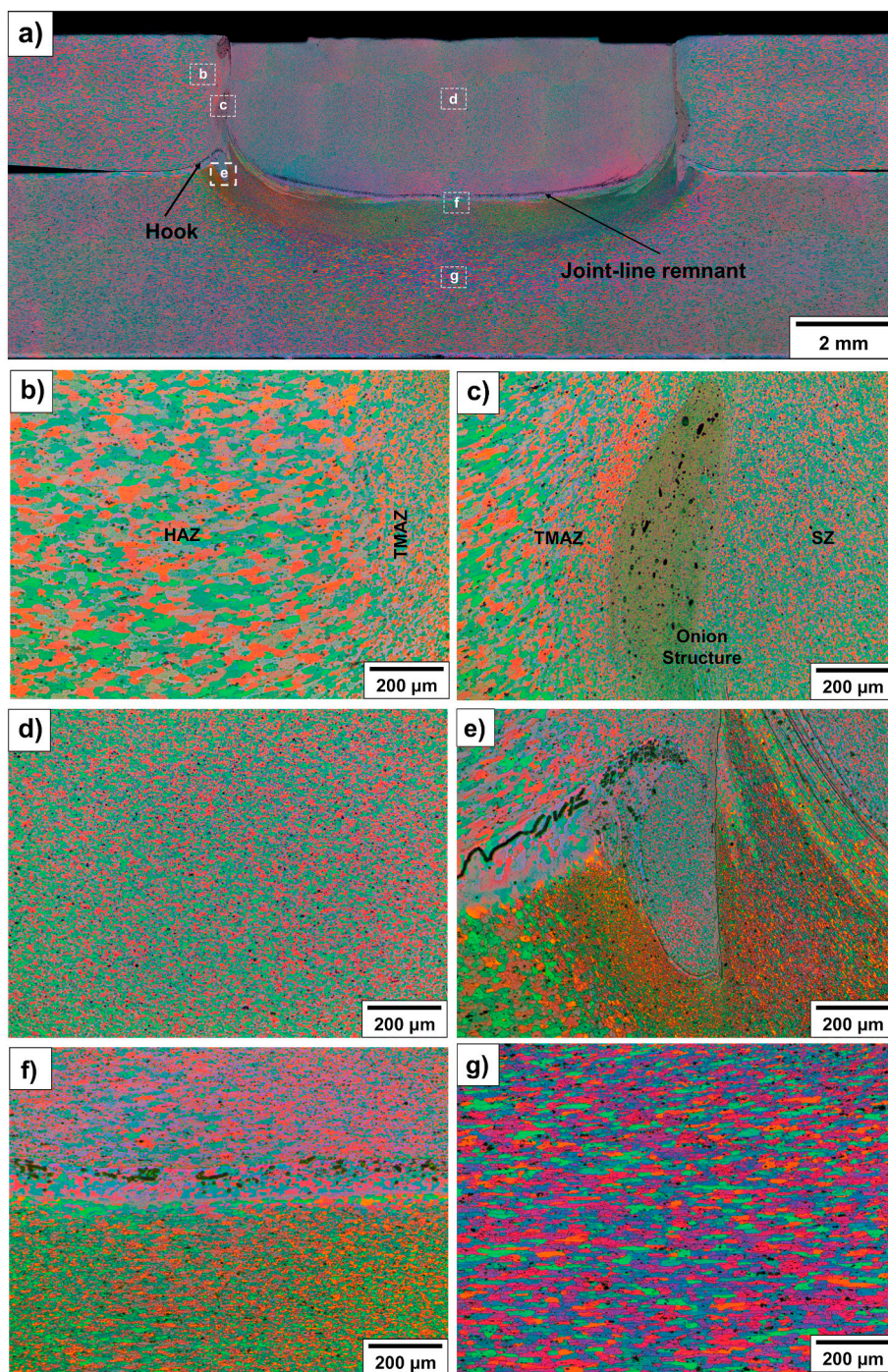

Fig. 5. a) Typical microstructures within the weld, produced with optimized process parameters: b) HAZ/TMAZ interface, c) TMAZ/SZ-P interface, d) SZ-S, e) region of shoulder tip influence, f) interface between 5A06-O/2219-T87 and g) center of AA2219-T87 sheet.

3.2. Microstructure characterization

From this section, welds produced by optimized parameters will be considered. The typical cross-section of the 5A06-O/2219-T87 refill friction stir spot weld, and its characteristics zones are shown in Fig. 5. Fig. 5a indicates no defects such as lack of refill or voids. The stir zone (SZ), thermo-mechanically affected zone (TMAZ), heat affected zone (HAZ) and, moreover, some geometrical features such as hook, and joint-line remnants can also be observed. The joint-line is a fine remnant oxide layer, a region with good adhesion between top and bottom sheets, resulting in satisfactory mechanical resistance [33,36]. Hook is a refill FSSW inherent feature that results from the bending of the sheet. In addition, hook also corresponds as a partial joint region and as a transition from the interface region of the non-welded overlapped sheets to the completely welded region, being considered as a partially bonded zone [36].

Fig. 5b shows the transition between HAZ and TMAZ. HAZ is characterized by slightly grain coarsening in comparison to base material because of the thermal cycle during the process. TMAZ undergoes plastic deformation and thermal cycle, but in lower levels regarding SZ; transition structure between TMAZ and SZ is seen in Fig. 5c. This structure is called onion structure, as reported by Cao et al. 40,41 in their study of 5A06 and 6061, formed during the plunging stage and corresponds to a mixture of 5A06 and AA2219. SZ undergoes severe plastic deformation, in addition to high temperatures caused by the friction between the tool and the material; dynamic recrystallization is favored, resulting in a microstructure composed of fine and equiaxial grains. SZ is divided into two different regions: stir zone affected by shoulder (SZ-S) and stir zone affected by probe (SZ-P). According to Xu et al. [31], as a consequence of different material flow and plastic deformation levels during the process, the SZ-S (Fig. 5d) usually shows smaller grain sizes in comparison to the SZ-P (Fig. 5c). This feature can be observed in Fig. 5e, where the plunging region of the shoulder is exactly demarcated. This region experienced the highest plastic deformation during the process, being possible to visualize extremely refined equiaxial grains. Furthermore, around this region it is also possible to observe a very complex microstructure with different grain sizes and morphologies, i.e., both recrystallized and elongated/deformed grains.

Fig. 5f shows the center interface between the sheets, where some black fragments (joint-line remnant) and a layer with partially recrystallized grains are seen. The middle of 2219 sheet is shown in Fig. 5g. Compared to its BM microstructure, the grain size increased in this region. Even though the tool did not penetrate until the middle thickness of the AA2219 sheet, the heat input generated in the process affects the microstructure.

The onion structure observed in Fig. 5e represents a microstructural feature that is not extensively reported in the literature, especially in the context of refill friction stir spot welding (FSSW). To gain a deeper understanding of its characteristics, Transmission Electron Microscopy (TEM) was employed to analyze this region in detail, as shown in Fig. 6.

The TEM analysis reveals a complex microstructure within the onion structure. Fig. 6a shows a bright-field (BF) TEM micrograph that highlights a variety of precipitates distributed along grain boundaries and within the grains. These precipitates are believed to play a crucial role in the mechanical properties of the weld, acting as strengthening phases or influencing grain boundary behavior. High-magnification TEM micrographs (Fig. 6b–g) provide closer views of the specific precipitates within the onion structure. These images reveal variations in size, morphology, and distribution of the precipitates, which likely originate from the intense thermal and mechanical conditions experienced during the welding process. The interface regions between grains also show evidence of nanoscale features, indicating localized deformation and recrystallization.

The electron nanodiffraction patterns in Fig. 6h and i, corresponding to selected precipitates from Fig. 6b and e, respectively, further confirm their crystalline structures. These patterns suggest that the precipitates are likely intermetallic compounds or secondary phases formed due to the interaction of 5A06-O and 2219-T87 alloys during the process. Energy-dispersive X-ray spectroscopy (EDX) analysis, shown in Fig. 6j, provides compositional information about the precipitates and surrounding matrix. The atomic percentages of the key elements indicate a complex chemistry in the onion region, influenced by the mixing and
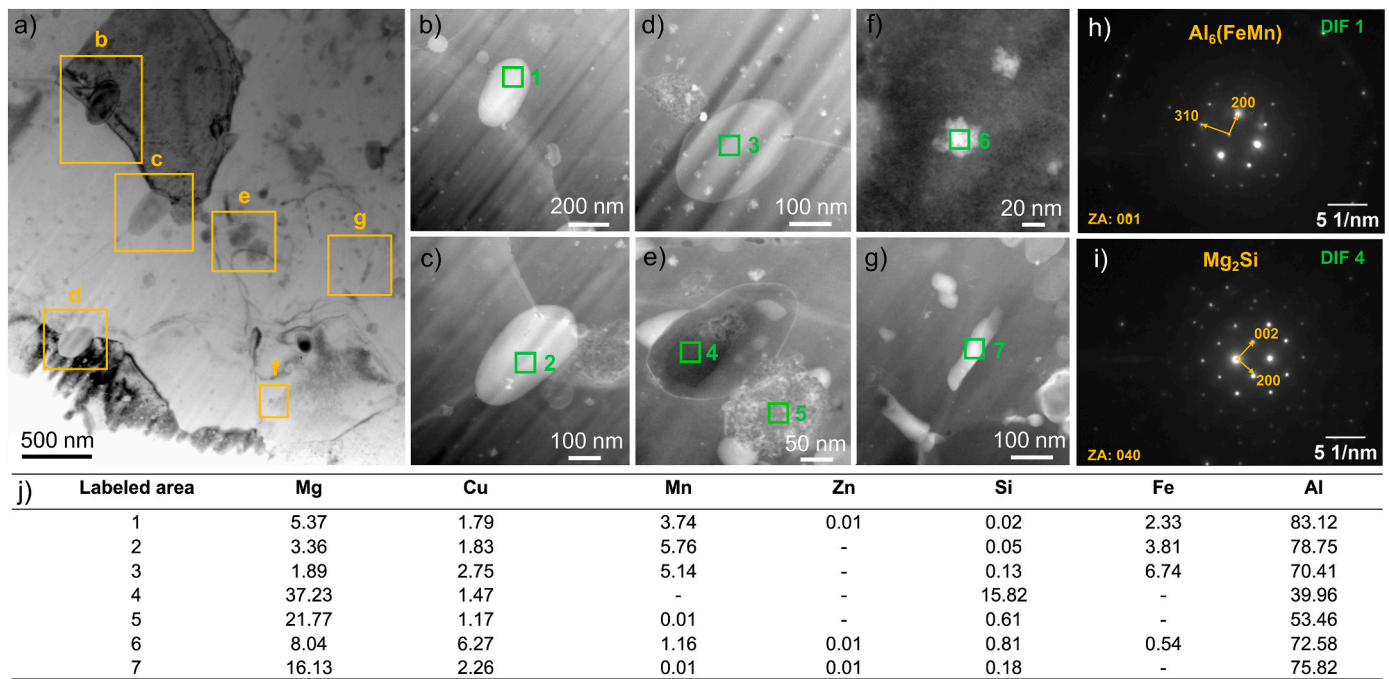

j)	Labeled area	Mg	Cu	Mn	Zn	Si	Fe	Al
	1	5.37	1.79	3.74	0.01	0.02	2.33	83.12
	2	3.36	1.83	5.76	-	0.05	3.81	78.75
	3	1.89	2.75	5.14	-	0.13	6.74	70.41
	4	37.23	1.47	-	-	15.82	-	39.96
	5	21.77	1.17	0.01	-	0.61	-	53.46
	6	8.04	6.27	1.16	0.01	0.81	0.54	72.58
	7	16.13	2.26	0.01	0.01	0.18	-	75.82

Fig. 6. Transmission electron microscopy (TEM) micrographs of the onion region within the weld. (a) A bright-field (BF) TEM image shows various precipitates distributed along the grain boundaries and within the grains. (b–g) High-magnification TEM micrographs provide detailed views of the precipitates identified in panel (a). (h, i) Electron nanodiffraction patterns are shown for the regions labeled in panels (b) and (e), respectively. (j) Energy-dispersive X-ray spectroscopy (EDX) analyses, presented in atomic percentages, details the chemical composition of the regions highlighted in panels (b–g).

diffusion of alloying elements from both sheets. Notably, the EDX results highlight the presence of elements such as Cu, Al, and Mg, suggesting that the precipitates may correspond to phases like Al–Cu–Mg compounds commonly found in similar alloy systems.

The microstructural features within the onion region are a result of the combined effects of severe plastic deformation and elevated temperatures during the plunging stage of the refill FSSW process. This distinctive microstructure, characterized by fine equiaxed grains and a diverse array of precipitates, plays a crucial role in influencing the weld's mechanical properties, including hardness, which will be discussed in detail later.

During the process, because of material flow caused by the tool motion, some layers might appear, as shown in Fig. 7. The AA2219 and 5A06 are intermixed together on the shoulder path, near the hook region. No pattern on the layer's distribution was detected, but the AA2219 material is pushed up during the refilling stage as can be seen by the EDS mapping of Cu. Furthermore, these layers within the shoulder path are composed mainly by Al and Cu, both from the top surface of AA2219, and Mg from the 5A06 sheet. The anodized layer was broken and got scattered in the region affected by the shoulder, while in the region without shoulder contact it was preserved. Wen et al. [42] observed the presence of these intermixed layers in 2219/6056 welds produced by bobbin-tool FSW, and concluded that with increase of welding speed, the welded joints became weaker. This argument corroborates the observation in this study, when increasing the plunge speed, the lap shear strength decreased.

Fig. 8 shows the EDS mapping performed in the mid region of the joint-line remnant. Based on the major elements present in both alloys, Al and O were observed in the joint-line remnant, while Mg, Cu and Mn are present just in the base material. Al shows itself distributed in a layer along the joint-line remnant, while O is present with morphology of broken fragments because of the tool movement generated during the process. This Al layer is most likely the Alclad layer. Li et al. [14] evaluated the effect of the Alclad layer in terms of microstructure and mechanical properties of 2A12-T4 aluminum alloy processed through refill FSSW. This layer has an important role in tensile-shear properties of weld joint, depending directly on its length.

3.3. Thermal cycle analysis

Fig. 9a shows the thermal cycle of the weld produced with optimized process parameters. The temperature distribution was measured at three different positions, which correspond to the regions beneath the probe, the shoulder and the clamping ring. The maximum temperature was 498 °C at the weld center, i.e., in the region influenced by the probe. This temperature was reached when the shoulder reaches the preset maximum plunge depth (3.2 mm). This temperature is slightly higher than the maximum temperature obtained in the region underneath the shoulder, which was 488 °C. The temperature difference compared to the region of the clamping ring, which experienced 407 °C as the maximum temperature, was quite significant. This difference is expected since regions subject to deformation, especially during the plunging stage, show significantly higher temperatures. A serrated feature, Fig. 9b, can be found during the dwelling and refilling stages, probably related to a decrease in viscosity of the plasticized material, which leads to less generated frictional heat [43].

3.4. Microhardness

The microhardness profiles measured at middle thickness at different natural aging times for the optimized condition are shown in Fig. 10. Regarding 5A06 sheet, regions outside of the influence of the shoulder and probe did not show a significant variation, Fig. 10a, showing hardness values between 90 and 95 $HV_{0.1}$. This is expected, since 5A06-O is a non-heat-treatable alloy, meaning that its mechanical properties are mainly governed by grain structure rather than precipitate distribution. Even though the HAZ is exposed to high temperatures during welding, its microstructure did not change significantly compared to the BM microstructure as shown in Fig. 3. As aforementioned, an important feature is the presence of the onion structure (Fig. 5c), which presents localized hardness peaks near the shoulder's path, in which the values vary for the natural aging times. The onion structure, a peculiar microstructural feature formed during the refill FSSW process, plays a fundamental role in the observed hardness peak. This structure is characterized by fine equiaxed grains and a high density of nano-precipitates, which are a direct consequence of the intense thermal and
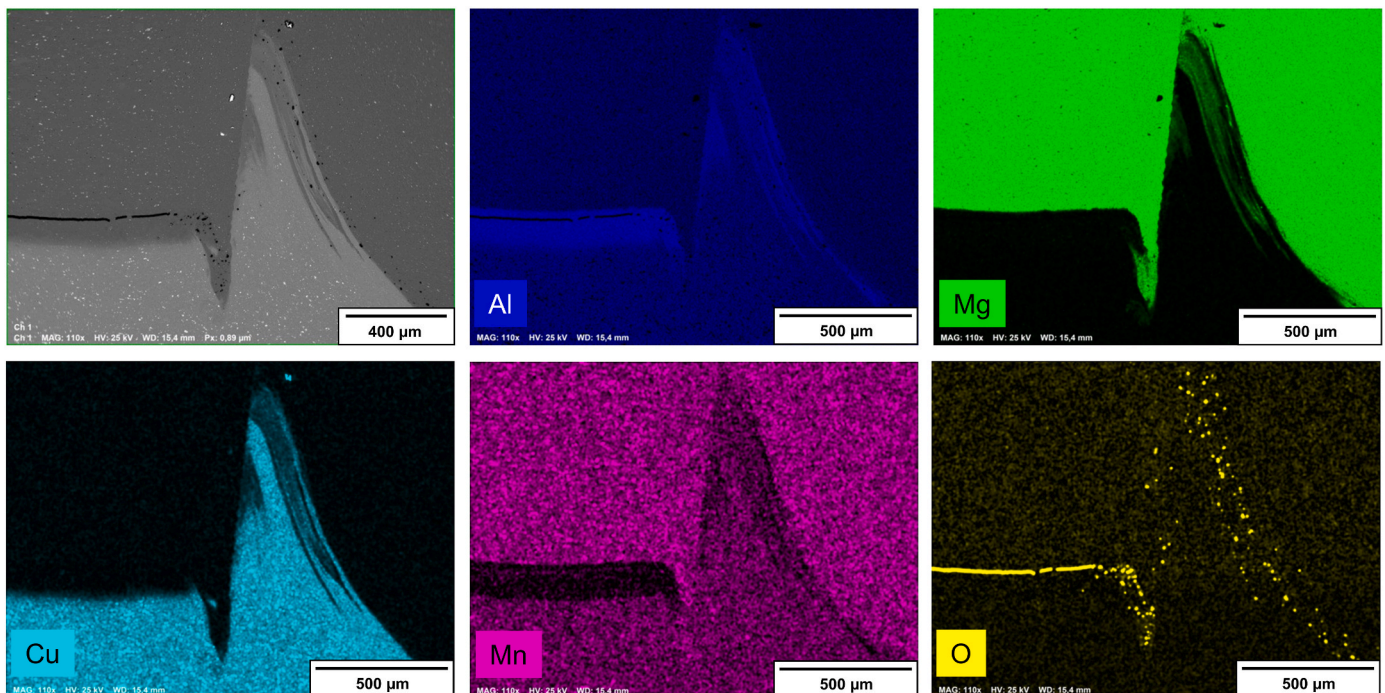

Fig. 7. Intermixed layers located on shoulder path for weld produced with optimized process parameters and EDS mapping of Al, Mg, Cu, Mn and O.
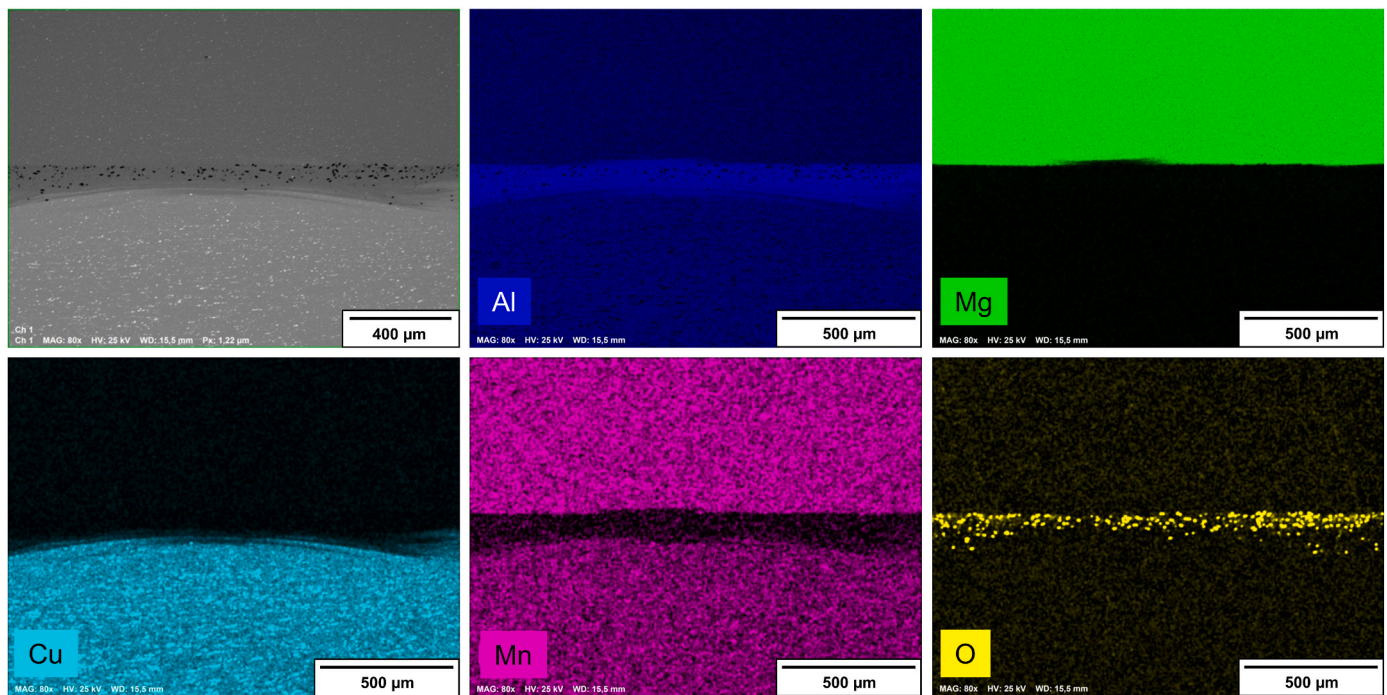
Fig. 8. Intermixed layers located on shoulder path for weld produced with optimized process parameters and EDS mapping of Al, Mg, Cu, Mn and O.
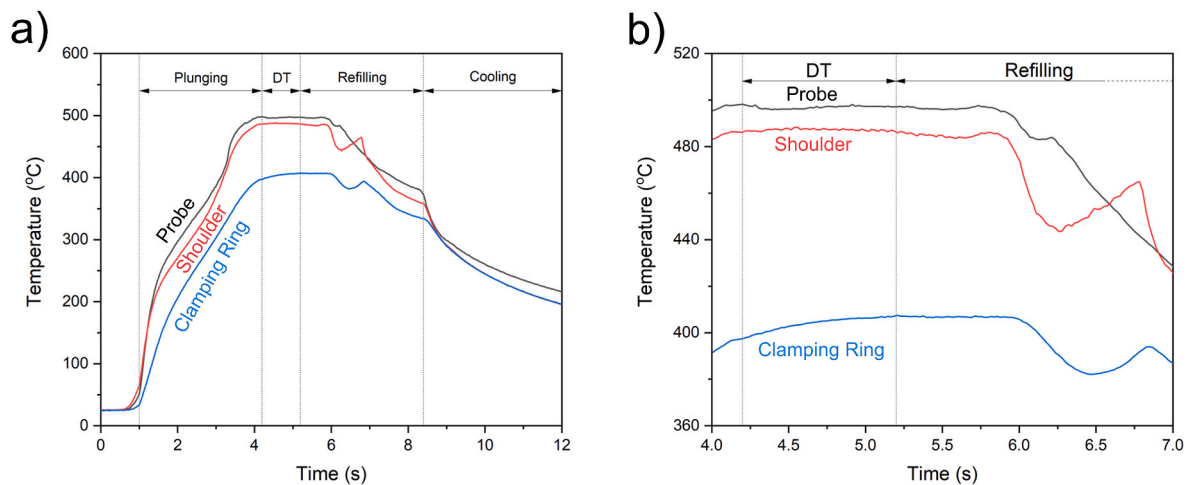

Fig. 9. a) Temperature distribution in different welding regions for the optimized welding parameters and b) highlighting of the serrated feature. DT = dwell time.

mechanical conditions imposed during the welding process. TEM analyses (Fig. 6) revealed that these precipitates are distributed both along grain boundaries and within the grains. It is suggested that these precipitates significantly enhance hardness by hindering dislocation movement, thus improving the strengthening of the weld and the material's resistance to plastic deformation. The hardness peaks associated with the onion structure can be attributed to the synergistic effects of both the refined grain structure and the precipitate strengthening mechanism. Therefore, the severe plastic deformation and elevated temperatures encountered during the plunging stage of the FSSW process are key factors that drive the formation of this distinctive microstructure, in which the high density of precipitates, combined with the grain refinement, grant substantial strengthening to the onion region, resulting in the highest hardness observed in this study. Thus, the onion structure is not only a characteristic feature of the weld but also a main contributor of its superior mechanical performance. Regarding natural aging, specimens in the as-welded and 1-day natural aged conditions

showed slight hardness variation, remaining around 105 $HV_{0.1}$ (see Fig. 10a). However, for 4-day and 7-day natural aged welds, the hardness significantly increases reaching approximately 130 $HV_{0.1}$, with 138 $HV_{0.1}$ as the maximum obtained value, which corresponds to a 37% increase in the hardness compared to the 5A06-O base material. The observed hardness evolution suggests that natural aging promotes precipitation hardening in 5A06-O, likely due to secondary precipitation phases.

On the other hand, the AA2219 sheet showed a significant decrease in hardness near the probe and shoulder regions (Fig. 10b). Since AA2219 is a heat treatable alloy, its mechanical properties strongly depend on the stability of its precipitates, the exposure to elevated temperatures during welding likely may be responsible for grains coarsening and dissolution of precipitates, which may lead to the material's softening. Although the thermal cycle has not been measured at the middle thickness of AA2219, Fig. 9 provides insight into temperature variations in different welding regions (underneath the clamping ring,

shoulder and probe). Therefore, the significant drop in hardness in AA2219 alloy suggests that the weld thermal cycle may have exceeded critical temperatures for precipitation stability, besides causing grain growth.

Therefore, the difference in hardness evolution between AA2219-T87 and 5A06-O is mainly due to their distinct strengthening mechanisms. AA2219-T87, being a heat-treatable alloy, relies on fine Cu-rich precipitates for strength. During welding, the localized high temperatures may dissolve or coarsen these precipitates, reducing their strengthening effect. Since natural aging at room temperature is not sufficient to effectively promote reprecipitation, the alloy remains softened after welding. In contrast, 5A06-O, a non-heat-treatable alloy, gains strength primarily through grain refinement and solid solution strengthening. The severe plastic deformation during welding leads to dynamic recrystallization and grain refinement, increasing hardness. Additionally, the gradual formation of precipitates in the onion structure over time can further contribute to strengthening, explaining the hardness increase observed after natural aging.

3.5. Stop-action experiments

In the following, the microstructure evolution during refill FSSW of 5A06/2219 is analyzed in terms of the performed stop-action experiments. In Fig. 11a, where the shoulder plunges only 1 mm in the top sheet, the grains in the SZ-P, and right below the SZ-S, begin to dynamically recrystallize, clearly visualizing the grain refinement in these regions compared to the BM grains. Furthermore, the grains in the shoulder's vicinity start to be smoothly rotated. Fig. 11b shows the cross section in the 2 mm plunge depth. As observed in Fig. 11a, the same microstructural features are present, but to a higher extent. Moreover, the grains in AA2219, right below the interface to the 5A06 sheet, were smoothly coarsened because of the thermal cycle generated by the process. Another point is the presence of voids in the region influenced by the probe. Since this test is abruptly interrupted, there is insufficient time for the material to properly fill the different regions of the weld.

For the stop-action experiment at 3 mm plunge depth, Fig. 11c, the tool reaches exactly the interface between the top and bottom sheet. Note that there is already a bond between them. However, at the test interruption, the top sheet has broken exactly in the region influenced by the outer surface of the shoulder. Furthermore, because of interruption, there was also a lack of refilling in the surface that was in contact with the probe surface. Since the plasticized material is forced to the cavity left by the probe during the process, some grains located in the central region, influenced by the probe, were not recrystallized. Another

feature that can be observed is the beginning of onion structure, being more visible in the region influenced by the outer surface of the shoulder.

In terms of the conventional refill process, Fig. 11d–f, the presence of volumetric voids on the shoulder path and lack of refill are seen, both starting to form in the first refilling stage and persist until the weld is completely formed, as can be clearly seen.

Fig. 11g–i shows the microstructures produced using 0.1 mm offset approach. Fig. 11g displays the cross section for this step after the tool has been retracted to 1 mm. Even though the refill FSSW process can produce weld with symmetric deformations, this feature becomes more apparent during the shoulder retraction, being possible to observe the different zones and their extents due to the tool movement. Furthermore, the joint-line remnant begins to form in a continuous way, differently from what was observed in Fig. 11c. Moreover, the hook starts to form during the shoulder retraction, very close to outer surface of the shoulder, i.e., even though there is no plunging in the bottom sheet, the presence of this geometric feature is inherent to the process and, as aforementioned, it has a direct influence to the shear strength of the weld and its morphology is mainly determined by the rotational speed and the plunge depth.

According to Hessel et al. [15], the hook configuration is mainly determined by the position and direction of material flow generated around the shoulder during plunging and refilling stages, being possible to have flat, downward and upward hook configurations. According to Zhang et al. [44], the downward flow of materials during FSW prevents cavity defects, with the hook typically bending upward under traditional FSLW conditions. However, in Offset FSLW (OF-FSLW), the hook bends downward due to the material concentrated zone (MCZ) above the lap interface. The cold lap morphology varies with tool design and rotational speed, with higher speeds compressing the cold lap into a bracket-shaped structure. Zhang et al. [45] have introduced the Impacting Flow FSLW (IF-FSLW) process, which uses an X-shape reverse-threaded pin to address the up-bending hook issue in traditional FSLW. This process creates a forky-structured hook through horizontal material flow and a downward-bending hook via vertical squeezing, significantly improving joint strength. The IF-FSLW joint achieved a tensile strength of 410 MPa and 92% joint efficiency, demonstrating its effectiveness in producing high-strength lap joints. These studies underscore the importance of material flow, tool design, and process parameters in controlling hook morphology and optimizing joint performance.

Fig. 11h and i reveal the cross section after the tool has been retracted 2 mm and the complete weld using the 0.1 mm offset,
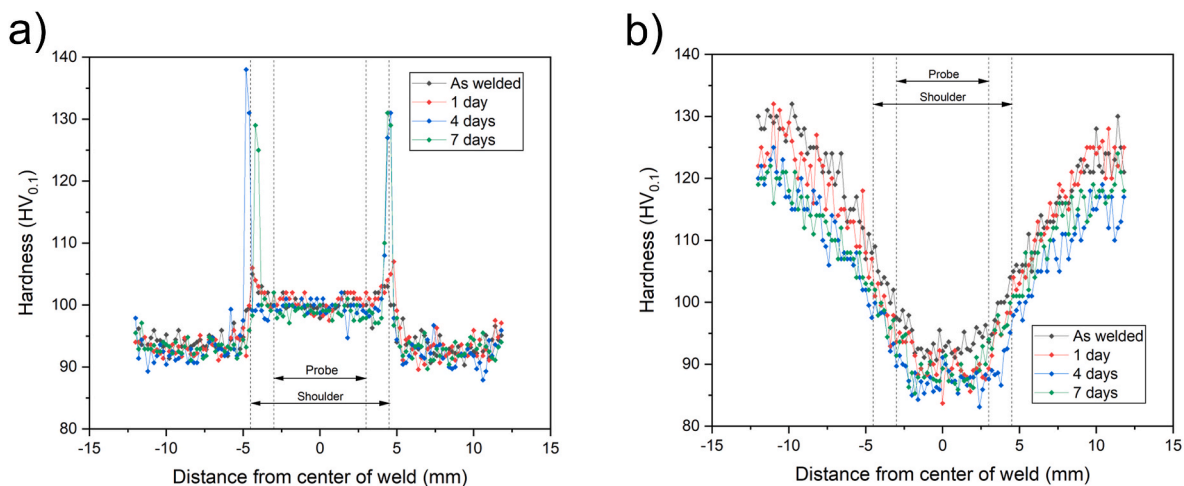

Fig. 10. Vickers microhardness of optimized condition weld for different natural aging times measured at a) middle-thickness of 5A06-O, b) middle-thickness of AA2219-T87.
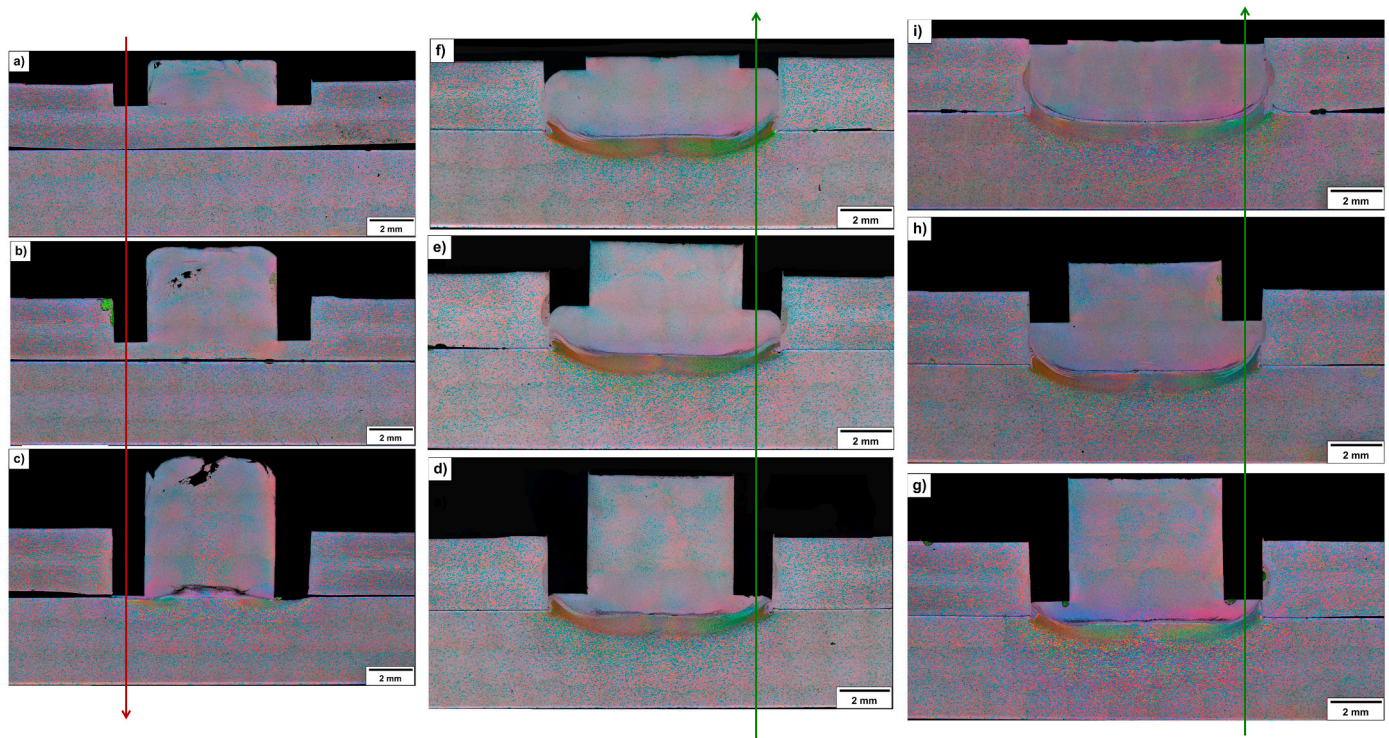
Fig. 11. Stop-action samples. Plunging stage interrupted at (a) 1 mm, (b) 2 mm and (c) 3 mm. Conventional refilling stage interrupted at (d) 2 mm, (e) 1 mm and (f) 0.1 mm. Refilling stage with 0.1 mm offset interrupted at (g) 2 mm, (h) 1 mm and (i) 0.1 mm.

respectively. In comparison to Fig. 11g, the main differences are the smooth increase in the zones and the trend of the joint-line remnant to keep even more concave due to the compression generated by the probe in the plasticized material during refilling stage. Moreover, for all the analyzed depth during plunging stage, there was complete and suitable filling of the weld with no defects such as lack of refilling and volumetric voids. As explained above, once the probe speed is increased through the modification of travel factor, this increase forces even more the

plasticized material to refill the cavities left by the shoulder during the retraction, producing defect-free welds with good quality.

3.6. Fracture analysis

Fracture morphologies of lap shear samples tested at room temperature were evaluated and are shown in Fig. 12, where the failure mode was always through the weld, i.e., the crack propagates through the
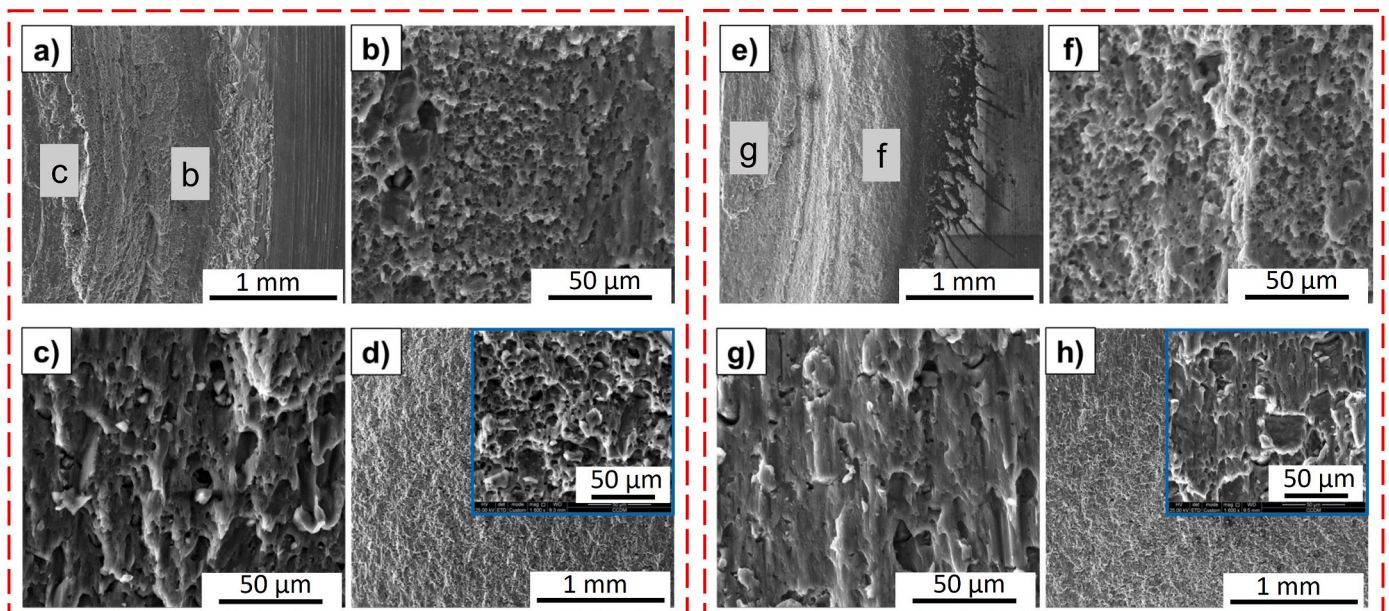

Fig. 12. Fracture surface after lap shear test at room temperature. The fractographies from (a) to (d), and from (e) to (h) correspond to 5A06 and 2219 sheets, respectively. (a, e) outer welding region, (b, f) region of influence of the outer shoulder surface, (c, g), region of influence of the internal shoulder surface, (d, h) central welding region.
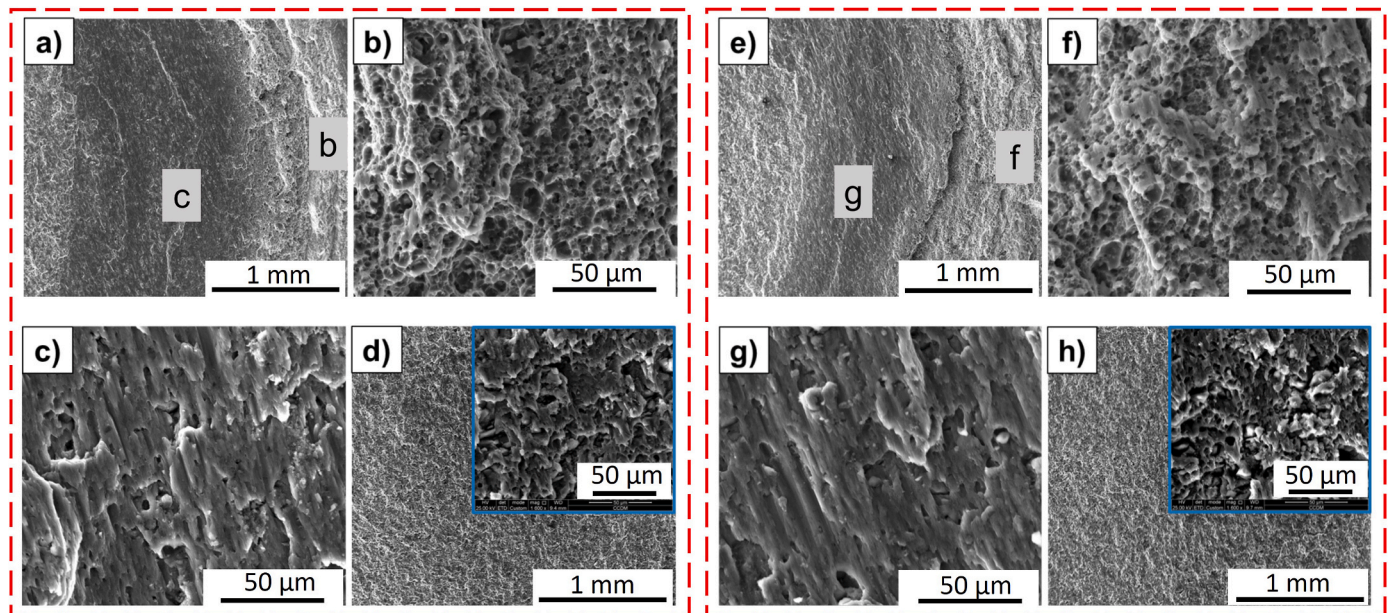
Fig. 13. Fracture surface after lap shear test at −55 °C. The fractographies from (a) to (d), and from (e) to (h) correspond to 5A06 and 2219 sheets, respectively. (a, e) outer welding region, (b, f) region of influence of the outer shoulder surface, (c, g), region of influence of the internal shoulder surface, (d, h) central welding region.

joint-line remnant. The crack starts at hook and propagates along the joint-line remnant. As aforementioned, the hook plays an important role in mechanical performance of the weld, and it is mainly determined by rotational speed and plunge depth. However, increasing the plunging depth could significantly decrease the LSS due to excessively curved profile of the hook. Fig. 12a corresponds to 5A06 sheet, and the marked regions are shown in higher magnification in Fig. 12b–d. As explained previously, the plastic deformation levels generated during the process are different along the joint. Fig. 12b reveals the presence of spherical dimples, indicating the occurrence of ductile fracture. According to Campanelli et al. [19], spherical dimples result from the growth of micro voids in the region of the sheet surface which is closest.

Fig. 12c presents the transition between the edge and the weld center with elongated dimples, a typical morphology of fracture surfaces subjected to shear loading. In the welding center, Fig. 12d, there is a mixture between elongated and spherical dimples. Furthermore, the presence of some second phase particles inside the spherical dimples was observed. Fig. 12e corresponds to the fractured surface of the bottom sheet using a lower magnification. As observed in the top sheet, there is a morphology transition from the outer region to the central region of the weld. Fig. 12f also exhibits plenty of spherical dimples, since this region was subjected to the highest shear loading. Elongated dimples can be observed in Fig. 12g, but with lower amount in comparison to Fig. 12c, likely due to the lower plastic deformation level of the bottom sheet compared to the top sheet. For the same reason, the central region of the AA2219 fracture surface, Fig. 12h, has shown just quite elongated dimples, differently of the observed morphology in the central region of 5A06 fracture surface (Fig. 12d). All these characteristics point out to a ductile fracture mode of the welds.

Fig. 13 presents the fracture surface after lap shear test at −55 °C. Fig. 13a reveals the fracture, with different morphologies for the outermost and innermost regions, indicated by letters **b** and **c**, respectively. Fig. 13b indicates a significant number of spherical dimples, since the highest plastic deformation level occurs on that, indicating a ductile fracture even for testing at −55 °C. The influenced region by the innermost part of shoulder, Fig. 13c, depicts elongated dimples, as observed in Fig. 12c. The central welding region, Fig. 13d, shows only smooth elongated dimples, differently from the features in Fig. 12d, spherical dimples were found as well. This is an indicative that, even if ductile, the specimen tested at −55 °C demonstrated a behavior less

ductile in comparison to the specimen tested at room temperature. Regarding the AA2219 sheet fracture surface, Fig. 13e–h, the morphology was quite like to that observed at room temperature. Fig. 13e corresponds to the influenced region by shoulder, being the regions marked by **f** and **g** as the outermost and innermost regions, respectively. As previously observed, the outermost, Fig. 13f, displayed a morphology constituted by spherical dimples, while the most internal region, Fig. 13g, presented quite elongated dimples, both indicating the occurrence of ductile fracture. The central region, Fig. 13h, shows morphology composed both by spherical and smooth elongated dimples, differently to the observed on the fracture surface of AA2219 tested at room temperature. To sum up, both at room and low temperatures (−55 °C), the welds fractured in ductile fashion, interesting to avoid catastrophic and fragile collapse upon loading in an extended temperature range.

4. Conclusions

This work investigated the welding parameters influence on LSS, thermal cycle, mechanical properties and microstructural characterization on refill friction stir spot welding of 5A06-O/2219-T87 welds. From the ensemble of the results and discussion, the following conclusions can be drawn.

1) Design of Experiments were performed through Box-Behnken Design. The most significant parameter on LSS was PD with 49.76% of contribution, followed by PS and RS with 15.52% and 9.70%, respectively.
2) The optimized process parameters settings were found to be RS = 2000 rpm, PS = 1 mm/s, PD = 3.2 mm and DT = 1 s. Employing this parameter setting, the average LSS at room and low temperature were 10.8 ± 0.6 kN and 11.9 ± 0.7 kN, respectively.
3) Microstructure shows typical welding zones and the geometrical features present in welds produced by refill FSSW: stir zone, thermo-mechanically affected zone, heat affected zone, hook and joint-line remnant. Furthermore, stop-action showed how the microstructure and defects are formed during the process.
4) The onion structure, featuring fine equiaxed grains and nano-precipitates, plays a key role in enhancing the weld's hardness. These precipitates, formed under the thermal and mechanical conditions of

the FSSW process, significantly strengthen the material within the onion structure.

5) The 0.1 mm offset has shown itself as a suitable configuration to produce defect-free welds for the 5A06/2219 joints, due to increasing travel speed.

6) The thermal cycle shows the maximum temperature during the plunging stage in the region influenced by probe, reaching 498 °C. The temperatures peaks in the region influenced by shoulder and clamping ring were 488 °C and 408 °C, respectively.

7) Through the weld failure mode was observed in lap shear tests both at room and negative temperatures. Spherical and elongated dimples were observed at the fractured surface, indicating ductile behavior.

8) In summary, this study not only enhances the understanding of Refill Friction Stir Spot Welding (RFSSW) in aluminum alloys but also underscores its significant potential for aerospace applications. The optimized welding parameters, defect-free joints, and superior mechanical properties demonstrate that RFSSW is a highly promising technique for manufacturing lightweight, high-strength propellant tanks and other critical aerospace components. These findings contribute to the advancement of safer, more efficient, and more reliable aerospace systems, meeting the industry's increasing demand for advanced joining technologies.

Declaration of competing interest

The authors declare that they have no known competing financial interests or personal relationships that could have appeared to influence the work reported in this paper.

Acknowledgements

References

[1] Guo N, Fu Y, Wang Y, Meng Q, Zhu Y. Microstructure and mechanical properties in friction stir welded 5A06 aluminum alloy thick plate. Mater Des 2017;113:273–83.

[2] Zhan X, Zhao Y, Liu Z, Gao Q, Bu H. Microstructure and porosity characteristics of 5A06 aluminum alloy joints using laser-MIG hybrid welding. J Manuf Process 2018;35:437–45.

[3] Peng G, Li L, Wang J, Xia H, Meng S, Gong J. Effect of subatmospheric pressures on weld formation and mechanical properties during disk laser welding of 5A06 aluminium alloy. J Mater Process Technol 2020;277:116457.

[4] He Hailin, Yi Youping, Huang Shiquan, Guo Wanfu, Zhang Yuxun. Effects of thermomechanical treatment on grain refinement, second-phase particle dissolution, and mechanical properties of 2219 Al alloy. J Mater Process Technol 2020;278:116506. https://doi.org/10.1016/j.jmatprotec.2019.116506.

[5] Kang J, Feng ZC, Frankel GS, Huang IW, Wang GQ, Wu AP. Friction stir welding of Al alloy 2219-T8: Part I-evolution of precipitates and formation of abnormal Al2Cu agglomerates. Metall Mater Trans A Phys Metall Mater Sci 2016;47(9):4553–65.

[6] Lei X, Deng Y, Yin Z, Xu G. Tungsten inert gas and friction stir welding characteristics of 4-mm-thick 2219-T87 plates at room temperature and -196 °C. J Mater Eng Perform 2014;23(6):2149–58.

[7] Arora KS, Pandey S, Schaper M, Kumar R. Microstructure evolution during friction stir welding of aluminum alloy AA2219. J Mater Sci Technol 2010;26(8):747–53.

[8] Li Q, Wu A, Li Y, Wang G, Yan D, Liu J. Influence of temperature cycles on the microstructures and mechanical properties of the partially melted zone in the fusion welded joints of 2219 aluminum alloy. Mater Sci Eng A 2015;623:38–48.

[9] Sivaraj P, Kanagarajan D, Balasubramanian V. Effect of post weld heat treatment on tensile properties and microstructure characteristics of friction stir welded armour grade AA7075-T651 aluminium alloy. Defence Technology 2014;10:1–8.

[10] Venugopal A, Sreekumar K, Raja VS. Stress corrosion cracking behavior of multipass TIG-welded AA2219 aluminum alloy in 3.5 wt pct NaCl solution. Metall Mater Trans A Phys Metall Mater Sci 2012;43(9):3135–48.

[11] Zhang C, Chang B, Tao J, Zhang T. Microstructure evolution during friction stir welding of 2024 aluminum alloy. Hanjie Xuebao/Transactions China Weld Inst. 2013;34(3):57–60.

[12] Shen J, Lage SBM, Suhuddin UFH, Bolfarini C, Santos JFDOS. Texture development and material flow behavior during refill friction stir spot welding of AlMgSc. Metall Mater Trans A 2018;49(1):241–54.

[13] Caroline C, Castro D, Henrique A, Pietta G, Guedes N, Alcântara D, et al. Investigation of geometrical features on mechanical properties of AA2198 re fi ll friction stir spot welds, vol. 36; 2018. p. 330–9.

[14] Li G, Zhou L, Luo L, Wu X, Guo N. Microstructural evolution and mechanical properties of refill friction stir spot welded alclad 2A12-T4 aluminum alloy 2019;8 (5):4115–29.

[15] Hessel B, Zepon G, Bolfarini C, Fernandez J. Materials Science & Engineering A Refill friction stir spot welding of AA6082-T6 alloy : hook defect formation and its influence on the mechanical properties and fracture behavior, vol. 773; 2020.

[16] Shen Z, Li WY, Ding Y, Hou W, Liu XC, Guo W, et al. Material flow during refill friction stir spot welded dissimilar Al alloys using a grooved tool. J Manuf Process 2020;49:260–70.

[17] Gera D, Fu B, Suhuddin UFHR, Plaine A, Alcantara N, dos Santos JF, et al. Microstructure, mechanical and functional properties of refill friction stir spot welds on multilayered aluminum foils for battery application. J Mater Res Technol 2021;13:2272–86.

[18] Shen Z, Ding Y, Chen J, Gerlich AP. Comparison of fatigue behavior in Mg/Mg similar and Mg/steel dissimilar refill friction stir spot welds 2016;92:78–86.

[19] Contri L, Fuad U, Suhuddin H, Ítalo A, Antonialli S, Fernandez J, et al. Journal of Materials Processing Technology Metallurgy and mechanical performance of AZ31 magnesium alloy friction spot welds. J Mater Process Tech. 2013;213(4):515–21.

[20] Suhuddin U, Fischer V, Kroeff F, Santos JF. Materials Science & Engineering A Microstructure and mechanical properties of friction spot welds of dissimilar AA5754 Al and AZ31 Mg alloys. Mater Sci Eng A 2014;590:384–9.

[21] Dong Z, Song Q, Ai X, Lv Z. E ff ect of joining time on intermetallic compound thickness and mechanical properties of re fi ll friction stir spot welded dissimilar Al/Mg alloys. J Manuf Process 2019;42:106–12.

[22] Plaine AH, Gonzalez AR, Suhuddin UFH, Santos JF, Alcântara NG. Materials & Design the optimization of friction spot welding process parameters in AA6181-T4 and Ti6Al4V dissimilar joints. Mater Des 2015;83:36–41.

[23] Plaine AH, Suhuddin UFH, Afonso CRM, Alcântara NG, Santos JF. Interface formation and properties of friction spot welded joints of AA5754 and Ti6Al4V alloys. JMADE 2016;93:224–31.

[24] Vacchi GS, Plaine AH, Silva R, Sordi VL, Suhuddin UFH, Alcântara NG, et al. Materials & Design E ff ect of friction spot welding (FSpW) on the surface corrosion behavior of overlapping AA6181-T4/Ti-6Al-4V joints, vol. 131; 2017. p. 127–34.

[25] Suhuddin UFH, Fischer V, Kostka A, dos Santos JF. Microstructure evolution in refill friction stir spot weld of a dissimilar Al–Mg alloy to Zn-coated steel. Sci Technol Weld Join 2017;22(8):658–65.

[26] Ferrari VR, Coury FG, Suhuddin UFH, Alcântara NG, dos Santos JF, Ohashi R, Fujimoto M, Koga GY. Effects of semi-solid structure on interface formation of dissimilar aluminum to galvanized steel welds produced by load-controlled Refill Friction Stir Spot Welding. J Manuf Process 2022;84:298–315.

[27] Chen Y, Chen J, Shalchi Amirkhiz B, Worswick MJ, Gerlich AP. Microstructures and properties of Mg alloy/DP600 steel dissimilar refill friction stir spot welds. Sci Technol Weld Join 2015;20(6):494–501.

[28] Shen Z, Ding Y, Chen J, Gerlich AP. Comparison of fatigue behavior in Mg/Mg similar and Mg/steel dissimilar refill friction stir spot welds. Int J Fatigue 2016;92: 78–86.

[29] Fu B, Shen J, Suhuddin UFHR, Pereira AAC, Maawad E, dos Santos JF, et al. Revealing joining mechanism in refill friction stir spot welding of AZ31 magnesium alloy to galvanized DP600 steel. Mater Des 2021;209:109997.

[30] Boldsaikhan E, Fukada S, Fujimoto M, Kamimuki K, Okada H. Refill friction stir spot welding of surface-treated aerospace aluminum alloys with faying-surface sealant. J Manuf Process 2019;42:113–20.

[31] Xu Z, Li Z, Ji S, Zhang L. Refill friction stir spot welding of 5083-O aluminum alloy. J Mater Sci Technol 2018;34:878–85.

[32] Zhao YQ, Liu HJ, Chen SX, Lin Z, Hou JC. Effects of sleeve plunge depth on microstructures and mechanical properties of friction spot welded alclad 7B04-T74 aluminum alloy. Mater Des 2014;62:40–6.

[33] Rosendo T, Parra B, Tier MAD, Silva AAM, Santos JF, Strohaecker TR, et al. Mechanical and microstructural investigation of friction spot welded AA6181-T4 aluminium alloy. Mater Des 2011;32(3):1094–100.

[34] Li Z, Gao S, Ji S, Yue Y, Chai P. Effect of rotational speed on microstructure and mechanical properties of refill friction stir spot welded 2024 Al alloy. J Mater Eng Perform 2016;25:1673–82.

[35] Ferreira AC, Campanelli LC, Suhuddin UFH, de Alcântara NG, dos Santos JF. Investigation of internal defects and premature fracture of dissimilar refill friction stir spot welds of AA5754 and AA6061. Int J Adv Manuf Technol 2020;106(7–8): 3523–31.

[36] Tier MD, Rosendo TS, Dos Santos JF, Huber N, Mazzaferro JA, Mazzaferro CP, et al. The influence of refill FSSW parameters on the microstructure and shear strength of 5042 aluminium welds. J Mater Process Technol 2013;213(6):997–1005.

[37] Chu Q, Li WY, Yang XW, Shen JJ, Vairis A, Feng WY, Wang WB. Microstructure and mechanical optimization of probeless friction stir spot welded joint of an Al-Li alloy. J Mater Sci Technol 2018;34(10):1739–46.

[38] Alaeibehmand S, Mirsalehi SE, Ranjbarnodeh E. Pinless FSSW of DP600/Zn/ AA6061 dissimilar joints. J Mater Res Technol 2021;15:996–1006.

[39] Fan W, Yang X, Chu Q, Li W. An efficient synergistic double-sided friction stir spot welding method: a case study on process optimization, interfacial characteristics and mechanical properties of 2198-T8 aluminum-lithium alloy joints. J Manuf Process 2024;131:213–32.

[40] Cao JY, Wang M, Kong L, Guo LJ. Hook formation and mechanical properties of friction spot welding in alloy 6061-T6. J Mater Process Technol 2016;230:254–62.

[41] Cao JY, Wang M, Kong L, Yin YH, Guo LJ. Numerical modeling and experimental investigation of material flow in friction spot welding of Al 6061-T6. Int J Adv Manuf Technol 2017;89(5–8):2129–39.

[42] Wen Q, Li W, Patel V, Bergmann L, Klusemann B, dos Santos JF. Assessing the bonding interface characteristics and mechanical properties of bobbin tool friction stir welded dissimilar aluminum alloy joints. Acta Metall Sin 2021;34(1):125–34.

[43] Suhuddin UFH, Fischer V, dos Santos JF. The thermal cycle during the dissimilar friction spot welding of aluminum and magnesium alloy. Scr Mater 2013;68(1). 97-90.

[44] Zhang Z, Jin Y, Ma L, Ji S, Dong J, Zhao H, Sun Z, Song Q. A general strategy for achieving high-strength joining of 2024 aluminum alloys via impacting flow friction stir lap welding. J Manuf Process 2025;134:619–32.

[45] Zhang Zhiqing, Gong Peng, Ji Shude, Ma Lin, Jin Chen, Li Xiuyan, Song Qi. Achievement of superb-strength lap joint via opposite-directions flowing friction stir lap welding of 2024 aluminum alloys. Chin J Aeronaut 2024. https://doi.org/10.1016/j.cja.2024.10.010. In press.